ELSEVIER

Journal of Hydrology 259 (2002) 32–48

Journal of Hydrology

www.elsevier.com/locate/jhydrol

On the use of combined geophysical methods to assess water content and water conductivity of near-surface formations

Stéphane Garambois*, Pascale Sénéchal, Hervé Perroud

Laboratoire d'Imagerie Géophysique, IPRA, CNRS UMR 5831, Université de Pau et des Pays de l'Adour, 64000 Pau, France

Received 29 September 2000; revised 16 October 2001; accepted 12 November 2001

Abstract

We propose to deepen the interpretation of combined geophysical methods (georadar, seismic and electric) to assess physical properties characterizing the near-surface porous formations, especially the influence of water. Velocity analysis of multioffset georadar data are used together with seismic methods to estimate lateral and vertical ground water fluctuations. This enables us to identify transitions from non-saturated to fully saturated porous layers with certainty. Furthermore, the accurate knowledge of seismic velocities helps to estimate the porosity of the ground water formations. Finally, we show how the radar technique may be useful in solving the problem of trade-off between bulk resistivity, which is deduced from electrical measurements, and that of water ionic conductivity and water content. These theoretical considerations are illustrated using various measurements conducted at the same test site. Our interpretation is compared with a few laboratory measurements on water and soil samples. This study displays the impact of combined geophysical approaches for providing models of water and ionic transfers down to a depth of several metres.

Keywords: Ground penetrating radar; Seismic and electrical methods; Water content; Water conductivity

1. Introduction

The knowledge of the geometry and the physical properties characterizing the subsurface is a contemporary challenge that society has increasingly to face, especially for ground water and its protection from sources of contamination of various kinds. Most physical properties of porous material (e.g. sedimentary rocks) are significantly influenced by the presence of water in pores and fissures and by their chemical properties (e.g. salinity). The use of classical, non-destructive, geophysical measurements should enable us to delineate changes of mineralogy, water content or chemistry and thus to develop optimum hydrological or geochemical investigations of the subsurface. The use of geophysical methods in such highly heterogeneous media is particularly problematic due to the fact that the physical parameters that can explain the observations are not unique, leading to an ambiguity in the interpretation. For example, seismic velocity variations can be due to changes in different physical properties (water content i.e. saturation, mineralogy, soil consolidation), thus making their interpretations ambiguous if there is no supplemental information. This problem can sometimes be reduced through the additional use of the multioffset ground penetrating radar (GPR) technique, its outcome (dielectric permittivity ϵ) being highly

* Corresponding author. Present address: LIRIGM, Université Joseph Fourier, 1381 rue de la Piscine, 38041, Grenoble Cedex 9, France. Tel.: +33-4-76-82-80-57; fax: +33-4-76-82-80-70.

E-mail addresses: stephane.garambois@ujf-grenoble.fr (S. Garambois), pascale.senechal@univ-pau.fr (P. Sénechal), herve.perroud@univ-pau.fr (H. Perroud).

0022-1694/02/$ - see front matter
PII: S0022-1694(01)00588-1

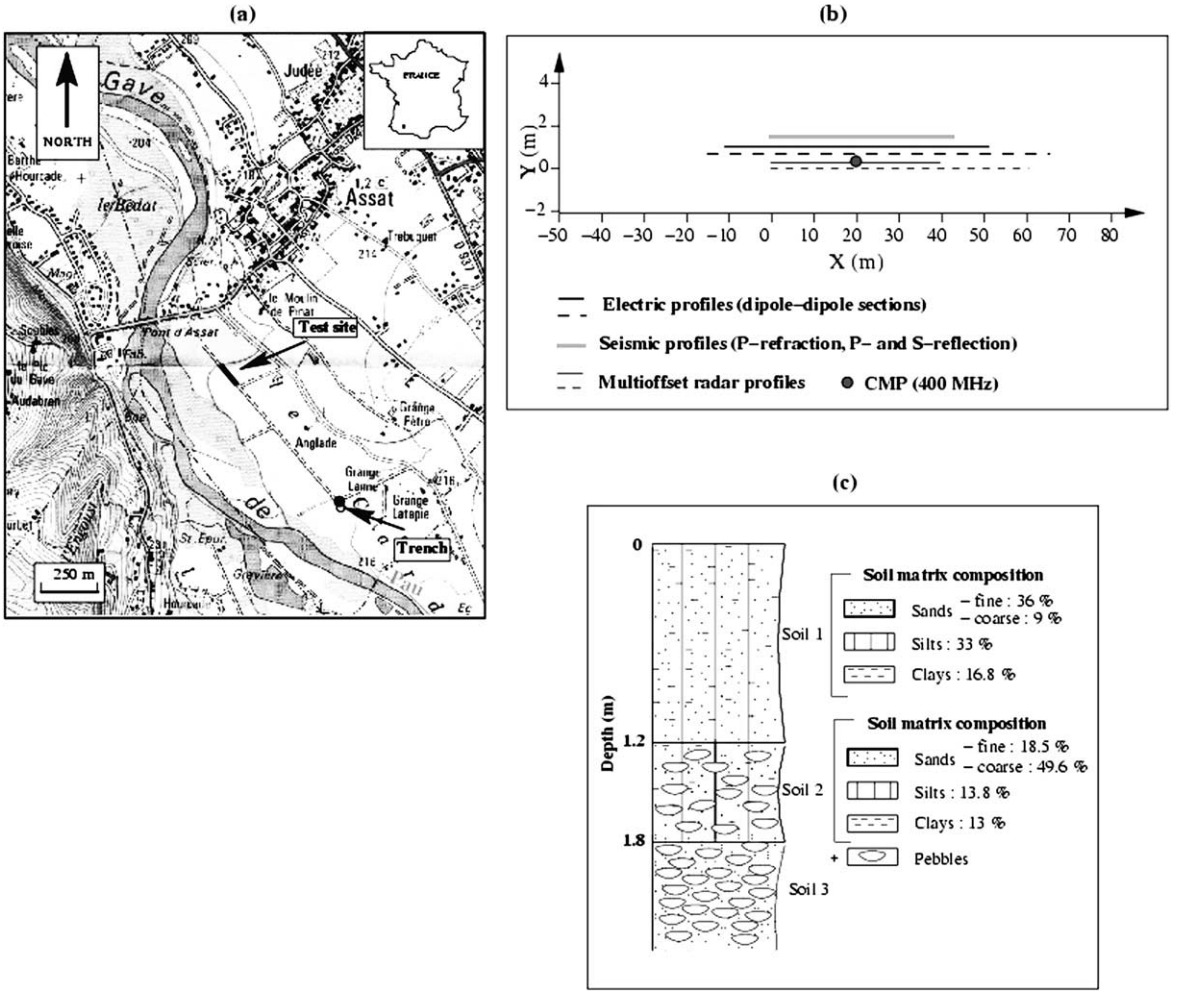

Fig. 1. (a) Test site location in the alluvial valley of the Gave de Pau river, in the South-West of France. (b) Location of the different geophysical profiles used in this study. The solid circle represents the location of the multioffset GPR section recorded using 400 MHz antennas at the middle of the 100 MHz multioffset GPR profile. Experiment A (solid line) was conducted in February 1999 and experiment B (dotted line) in December 2000. (c) Pedological log based on sample analysis of a trench located 600 m from the test site.

sensitive to the water content of granular sediments (Sen et al., 1981; van Overmeeren et al., 1997). As a matter of fact, several researches on the use of GPR as an in situ water detector have been published recently (e.g. Weiler et al., 1998; Dannovski and Yaramanci, 1999; Hagrey and Müller, 2000; Charlton, 2000).

The interpretation can be improved by combining information derived from different geophysical techniques. The approach presented here includes theoretical studies of the geophysical response linked to each individual geophysical technique (GPR, geoelectrics, and seismics) for unsaturated porous materials of the vadose zone. The main outcome is to estimate quantitatively the soil moisture content from GPR and to compare these estimates with supplementary techniques, which are used also to improve interpretation. It also underlines the advantage of combining results of GPR with the electrical methods to solve the problem of trade-off between bulk resistivity, water resistivity (salinity) and water content in Archie law. This allows us to create an image of water conductivity

variations (and possible anomalies), as well as possible ionic transfers in the soil.

The present studies are illustrated using geophysical data acquired at the Anglade test site, near Pau (South-West France) in the alluvial valley of the Gave de Pau river (Fig. 1a). The studied formation belongs to the recent Würm glaciation period and is mainly composed of coarse deposits of pebbles and sands. The water table varies from 1 to 5 m in depth, depending on the weather and season. The field work was carried out on a gravel track separating agricultural fields where fertilizers were applied. We conducted two experiments, the first in February 1999 (experiment A) consisting of seismic studies (P-wave refraction, P and S-wave reflection), multioffset GPR and dipole–dipole electrical profiles (Fig. 1b). The second experiment was conducted in December 2000 (experiment B), where GPR multioffset and dipole–dipole electrical profiles were carried out. For experiment B, we performed sample analysis, (1) of the water table in a nearby well (conductivity and characterization of the solute ions and cations), and (2) of a 1 m depth soil located at $x = +3$ m along the profile (conductivity, pH, clay composition, nitrates proportion). These independent measurements helped us to interpret some of the geophysical data. Beside this, a 2 m deep trench located in the same formation, but 600 m away from the acquisition site, allowed us to analyse the composition of the soil matrix in the laboratory. The hole drilled on the profile during experiment B (at $x = +3$ m) revealed almost the same geological formation, thus indicating that the trench soil analyses are representative of the test site where the geophysical measurements were acquired. The only deviation along our profile was the presence of gravel track material from the surface down to about 0.4 m depth.

Three types of soil layers, all of them presenting low clay contents (<17%), have been distinguished (Fig. 1c). The first layer, down to 1.2 m depth, consists of a mixture of very fine sands (44%), silts (33%) and clays (16.8%) and can be denoted loam (according to the textural triangle convention). The second layer, down to 1.8 m depth, is composed of sands (50% coarse sands + 18% of fine sands), mixed with silts (15.5%) and clays (13%) and is denoted sandy loam. It overlies a layer of pebbles (ophites, granites and quartzites) possessing a sandy matrix.

2. Water content estimations from GPR data

Microscopic fluid distribution can significantly affect dielectric properties of granular sediments. The GPR method has been used increasingly in the last few years to estimate directly the water content of near-surface rocks. For example, Greaves et al. (1996) showed field applications of multioffset GPR data and interpreted subsurface variations of volumetric water content quantitatively. van Overmeeren et al. (1997) showed that GPR can provide reliable quantitative informations of the soil water content from the surface, both vertically and horizontally, and so avoids drilling. Proof of this was established after comparing water content estimates obtained using GPR and from a capacitance probe. In the same way, Hagrey and Müller (2000) successfully investigated the capability of GPR to determine accurately the pore water content of clean sands, both in the laboratory and at outdoor experimental sites. In this section, we summarize the different steps allowing us to quantify the pore water content from GPR data. To be more specific, we (a) present briefly the dependence of the radar wave velocity on soil dielectric permittivity and associated assumptions, (b) address the data acquisition and processing steps required to determine radar velocities precisely, and (c) discuss different expressions relating the dielectric properties of rocks to their pore water content. Some of these steps are illustrated by our field examples.

2.1. Propagation velocity of radar waves

In general, the radar wave velocity depends on the dielectric permittivity ϵ, the magnetic permeability μ, and the electrical conductivity σ of the considered material, which are all complex and frequency-dependent tensor parameters.

Nevertheless, it has already been shown (e.g. Davis and Annan, 1989) that the radar wave velocity v can be approximated as

$$v = \frac{c}{\sqrt{\epsilon_r}} \tag{1}$$

where ϵ_r denotes the relative dielectric permittivity and c the velocity of free space. Relation (1) is valid for nearly homogeneous and isotropic formations and results from the hypothesis that $\epsilon = \epsilon_0 \epsilon_r$, where ϵ_0

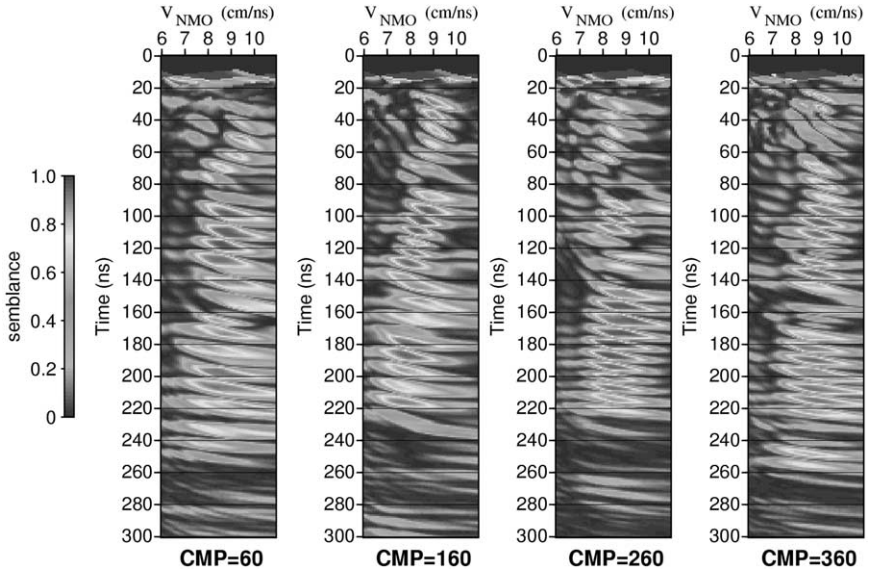

Fig. 2. Semblance panels obtained from four super-CMPs after preprocessing of GPR data collected at the test site (experiment A).

denotes the permittivity of free space ($=8.854\times10^{-12}$ F/m). The major assumptions leading to this approximation are (i) that the material is a good dielectric, i.e. the conduction current density is negligible compare to the displacement current density $[\sigma/\omega\epsilon_0\epsilon_r \ll 1]$, where ω is the angular frequency and, (ii) that the dispersive effects that appear through ϵ are negligible, which is usually the case in the 50–1000 MHz frequency range. The good dielectrics assumption for soils is often encountered in nature, especially when no metallic objects or minerals are present, or when rocks possess a low clay content. Considering our test site, inversion of electrical data, presented later, show resistivities in the range between 50 and 2250 Ohm m^{-1}. We used 100 MHz electric antennas for GPR data acquisition, and thus $\sigma/\omega\epsilon_0\epsilon_r \ll 1$. In any case, if this assumption was not satisfied, there would be no strong reflected waves on GPR sections.

An important consequence is that the GPR wave velocity is invariant in this frequency range, depending only on the dielectric constant of the medium of propagation.

However, as pointed out by Greaves et al. (1996), in addition to the major assumptions discussed before, some other factors have been omitted. These include scattering losses and possible signal variations caused by the technique used. Nevertheless, such possible disturbances are expected to produce second-order effects, as compared to velocity variations in the ground, especially when strong reflections are found on GPR sections.

2.2. Electromagnetic velocities derived from GPR data

The common mid point (CMP) soundings, obtained by varying the radar antenna spacing at a fixed central location and measuring the change in the two-way traveltime to the reflectors, can be used to determine a 2D stacking velocity field. In the CMP configuration, this stacking velocity field is extracted from normal-moveout velocities deduced from standard reflections analysis applied to radar waves (e.g. Yilmaz, 1987).

The corresponding detailed processes are now described and discussed.

2.2.1. GPR processing

The GPR measurements were conducted using a RAMAC/GPR unit system (MALA Geosciences) connected to 100 MHz antennas. For experiment A, radar data were collected with a set of 8 transmitters to receiver offsets, ranging from 1 to 8 m, such that, after

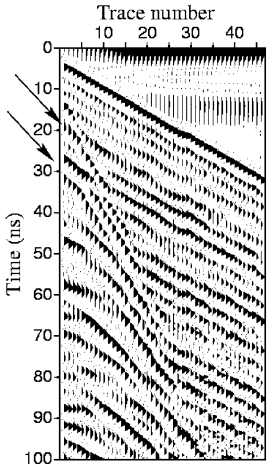

Fig. 3. 400 MHz antennas CMP gather used to support the resolution of the NMO velocity model in the first layer (experiment A). Two reflected waves are identified at approximately 19 and 29 ns (arrows).

re-arrangement, 401 CMPs of 8 traces spaced every 0.1 m on a 40 m long profile were available. For experiment B, CMP radar data were recorded every 4 m on a 60 m long profile with transmitter to receiver offsets ranging from 0.6 to 10 m, every 0.2 m.

Some preprocessing steps needed to be applied to the data before velocity analysis. To reduce noise and undesirable signals, a 15–250 MHz zero-phase bandpass filter was applied to the data, followed by a top mute of first arrivals corresponding to the direct waves. Next, the amplitudes were normalized by dividing each trace of a constant offset section by the average of the envelope traces of that section. For experiment A, the normal moveout was analysed in a first stage using the semblance maxima approach. Such an approach, well-known in seismic processing (Yilmaz, 1987), yields the stacking normal moveout (NMO) velocity V_{NMO}, that provides the normal moveouts appropriate for the offsets of the traces being examined as a function of arrival time. The semblance between the traces is determined, and this process is repeated until the semblance has been determined as a function of both stacking velocity and arrival time. To improve the picking resolution in the velocity spectra, traces from a few gathers around each CMP chosen for velocity analysis were combined (super-CMP). Fig. 2 displays the semblance panels of 4 chosen super-CMP collected at the Anglade test site (Exp. A), obtained after combining traces from 7 CMP gathers (for the entire profile, this process has been repeated every 20 CMP gathers, i.e. every 2 m). For each super-CMP, the NMO velocity of each reflector was determined using the maximum corresponding semblance. The studied reflections are mainly between 45/50 ns and 240 ns, and are associated to NMO velocities between 7.6 and 9.6 cm/ns. A difficulty of this approach concerns the velocity spreading of the semblance, associated to the stretching effect of the NMO correction. The second stage of the process to refine these estimates consists of superimposing the hyperbolae corresponding to the obtained NMO velocities on the central CMP gather. This was done to refine the fit with the GPR data (if necessary), which improves the precision to ± 0.2 cm/ns. Another problem concerns the lack of information until 45 ns, which is principally due to the fact that at 100 MHz reflected waves destructively interfere with the direct wave propagating in the ground, which can lead to substantial errors in the interval velocity estimates. To overcome this problem, one can use higher frequency antennas, which can provide more information on superficial layers. Fig. 3 shows a 400 MHz central acquisition CMP gather, where reflected waves appear at approximately 19 and 29 ns. The corresponding NMO velocities have been added to the NMO velocity model with the assumption that they are laterally constant along the entire profile. Fig. 4a shows the resulting 2D NMO velocity field obtained from interpolation of the various 1D velocity models computed for every 20 CMP gathers. The NMO velocity field has been superimposed on the stacked CMP section (described in the next paragraph) to show the consistency between reflections and velocity variations. The 2D model appears relatively smooth, and artifacts due to the poor resolution of semblance spectra have been removed.

After applying the normal-moveout corrections computed using the derived 2D NMO velocity field, the multioffset data were stacked to produce the simulated zero offset section shown in Fig. 4b. In comparison to single-channel recordings, the stacking step has improved the signal-to-noise ratio significantly. It has also increased the depth of penetration and the quality of interpretation of structural and stratigraphic details (Fisher et al., 1992).

The same analyses were performed to derive the

NMO velocity model corresponding to the experiment B (which is not presented here) except that we obtained near-surface lateral variations without using higher frequency antennas. This was possible thanks to the larger number of traces available in every CMP, making the recognition of the first reflections possible. In addition, the larger number of traces results in a higher confidence in NMO velocity estimates (±0.05 cm/ns).

2.2.2. Interval velocity

The average interval velocity $V_{i,j}$ between times t_i and t_j, can be computed from the NMO velocity using the Dix formula (Dix, 1955)

$$V_{i,j}^2 = \frac{V_{\mathrm{RMS},j}^2 t_j - V_{\mathrm{RMS},i}^2 t_i}{t_j - t_i}; \quad i = 1, 2, \ldots, n-1; \; j = i+1. \tag{2}$$

Here $V_{\mathrm{RMS},j}$ is the NMO velocity at zero-offset arrival time t_j, corresponding to the jth reflection. The use of this formula is only valid for almost horizontally stratified media, which is approximately the case for our test site (see Fig. 4b). Application of this formula (classical in seismic processing) can provide non-real velocities, if the traveltime intervals are small or if the NMO velocity change is large. Such problems were not encountered in our case. The obtained interval velocities after smoothing are presented in Fig. 4c and d for experiments A and B, respectively. Both figures show relatively similar velocity sections, ranging from 6 to 11 cm/ns, that consist of successive horizontal layers. From top to bottom we can distinguish on Fig. 4c a moderate velocity layer (<8.5 cm/ns) between 0 and 1.2 m depth, followed by a high velocity layer (>9 cm/ns) between 1.2 and 2.5 m depth overlying a low velocity layer (between 5 and 8 cm/ns). The latter presents substantial lateral variations. For experiment B, the first layer does not appear so clearly, as it presents lateral variations. The second layer seems to be thicker down to 3 m depth and the low velocity layer appears more homogeneous than the one deduced from experiment A. The reliability of both models depends on the accuracy of the NMO velocity estimates based on the Dix formula. We shall see in Section 2.3 how this 2D velocity field can be used to estimate the water content in the layers.

2.3. Sensitivity of the dielectric permittivity to the water content

The effective dielectric constant of a porous material is highly sensitive to its volumetric water content θ because the relative dielectric constant of water ($\epsilon_{\mathrm{r,w}} \simeq 80$) is several orders in magnitude higher than the dielectric constant of most minerals forming a rock matrix ($\epsilon_{\mathrm{r,g}} = 3-5$) and of air ($\epsilon_{\mathrm{r,a}} = 1$). Thus, the knowledge of the variations of the dielectric constant allow the determination of the water content distribution in the soil.

Several models can be found in literature (e.g. Sen et al., 1981; Shen et al., 1985) that propose a relationship between the dielectric constant and properties characterizing the water content θ, i.e. porosity ϕ and water saturation S_{w} ($\theta = \phi S_{\mathrm{w}}$). This relation can be derived from capillary tube or network models and from percolation and effective medium theories.

One such formula is derived from the electromagnetic analogue of the time-average Wyllie equation for seismic velocities, and is known as the complex refractive index method (CRIM, Freedman and Vogiatzis, 1979). As pointed out by Dvorkin and Nur (1998), this approach consists of simply assuming that the total traveltime of a wave (seismic or electromagnetic) in a multicomposite medium is the sum of the traveltimes along the individual components (as if the components were arranged in layers normal to the direction of propagation and the wavelengths were small compared to the thickness of an individual layer). For a water–air–mineral mixture, this model leads to the dielectric constant

$$\sqrt{\epsilon_{\mathrm{r}}} = (1-\phi)\sqrt{\epsilon_{\mathrm{r,g}}} + \phi S_{\mathrm{w}}\sqrt{\epsilon_{\mathrm{r,w}}} + \phi(1-S_{\mathrm{w}})\sqrt{\epsilon_{\mathrm{r,a}}}, \tag{3}$$

where subscripts g, w and a denote grain, water and air respectively. The major problem with the above relationship is that it does not take into account the geometrical information on the internal structure of rocks and on microscopic fluid distribution. As shown in Endres and Knight (1992), this has a significant effect on dielectric properties of partially saturated rocks. The above restriction may be overcome

by using another differential mixing expression, the Hanai–Bruggeman formula. It allows the determining of (1) the effective relative dielectric constant of a water/air mixture $\epsilon_{r,w/a}$, and (2) the effective relative dielectric constant of the total rock by mixing the mineral grains into the water/air mixture. The resulting relative dielectric constant is found to be

$$\epsilon_r = \epsilon_{r,w/a}\phi^{m_2}\left(\frac{1-\frac{\epsilon_{r,g}}{\epsilon_{r,w/a}}}{1-\frac{\epsilon_{r,g}}{\epsilon_r}}\right)^{m_2}, \quad (4)$$

$$\epsilon_{r,w/a} = \epsilon_{r,w}S_w^{m_1}\left(\frac{1-\frac{\epsilon_{r,a}}{\epsilon_{r,w}}}{1-\frac{\epsilon_{r,a}}{\epsilon_{r,w/a}}}\right)^{m_1}. \quad (5)$$

Here m_1 and m_2 are the cementation exponents. m_1 is related to the microgeometry of the water/air mixture that fills the pore space and may vary with the level of water saturation (Endres and Knight, 1992) whereas m_2 is related to the shape of the mineral grains. The main problem with the two previous approaches is that it is not possible to derive both the porosity and the water content from the dielectric constant. We cannot therefore obtain information about the water content without strong a priori assumptions. For this reason, it is preferable to use the well-known empirical equation derived in Topp et al. (1980) regarding the study of the dielectric response ϵ_r of various soil samples (presenting different degrees of saturation), as a function of their net water content θ. This formula is given by

$$\epsilon_r = 3.03 + 9.3\theta + 146.0\theta^2 - 76.7\theta^3. \quad (6)$$

Topp et al. (1980) propose a reciprocal expression for estimating θ in terms of a polynomial function in ϵ_r

$$\theta = -5.3\times10^{-2} + 2.92\times10^{-2}\epsilon_r - 5.5\times10^{-4}\epsilon_r^2 + 4.3\times10^{-6}\epsilon_r^3. \quad (7)$$

Greaves et al. (1996) compared the results predicted by the Hanai–Bruggeman formula (4) with those predicted using the Topp relation (7), and noted the good correlation between the two models. Greaves et al. (1996) considered the cementation exponent to vary from $m_1 = 2$ to $m_1 = 1.5$ when the water saturation increases. In practice, m_2 is related to the grain shape and varies from 1.5 (well-rounded grains) to more than 2 (oblate grains).

The three models presented above, directly expressing the dielectric constant as a function of the porosity and the water saturation, have been applied to the data recorded in our Anglade test site. The 2D velocity models presented in Fig. 4c and d have already been converted into dielectric constant models using Eq. (1). Fig. 5a displays 2D estimates of the volumetric water content θ for experiment A using (a) the Topp empirical relation (7), (b) the CRIM formulation in a saturated porous medium (Eq. (3), with $S_w = 1$), and (c) the Hanai–Bruggeman relation in a saturated porous medium with $m_2 = 1.5$ (Eqs. (4) and (5), with $S_w = 1$). The choice of m_2 comes from the analysis of samples down to 2 m depth (Fig. 1c), which shows the predominance of well-rounded unconsolidated sand grains or gravels. The three models show similar estimations on the water content of the medium (see legend colour axis), except when it drops to low values. In this case, the approximation of fully saturated material seems to be less valid, and only the Topp relation should be considered. For experiment B, we present on Fig. 5b only the results obtained using the Topp empirical relation (7).

Fig. 5a displays a first layer going from surface to

Fig. 4. (a) Superimposition of the 8-fold stacked CMP section with the 2D NMO final velocity model obtained after semblance analysis, hyperbola adjustment and 400 MHz central CMP analysis (experiment A). (b) Unmigrated 8-fold stacked CMP section (offsets from 1 to 8 m). (c) and (d) Final interval velocity 2D model obtained from the NMO velocity model using the Dix formula for experiments A and B, respectively.

Fig. 5. (a) Water content estimates from the velocity analysis of multioffset GPR data for experiment A. The colour bars display whether the water content has been estimated using the Topp equation or from the water-saturated CRIM or Hanai–Bruggeman ($m = 1.5$) equations. In the last two cases, the volumetric water content is equal to the material porosity. (b) Water content estimates for experiment B, using only the Topp equation.

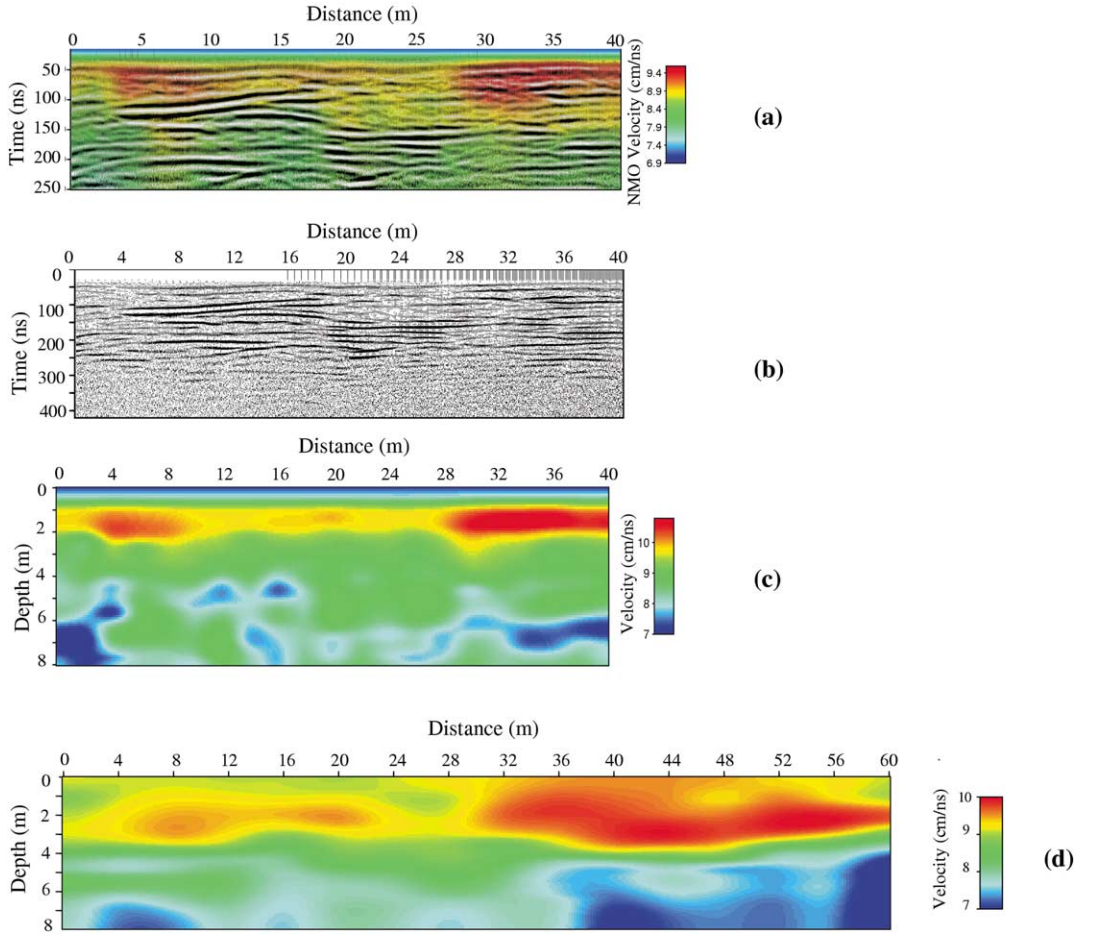
Distance (m)
Time (ns)
NMO Velocity (cm/ns)
(a)
Distance (m)
Time (ns)
(b)
Distance (m)
Depth (m)
Velocity (cm/ns)
(c)
Distance (m)
Depth (m)
Velocity (cm/ns)
(d)

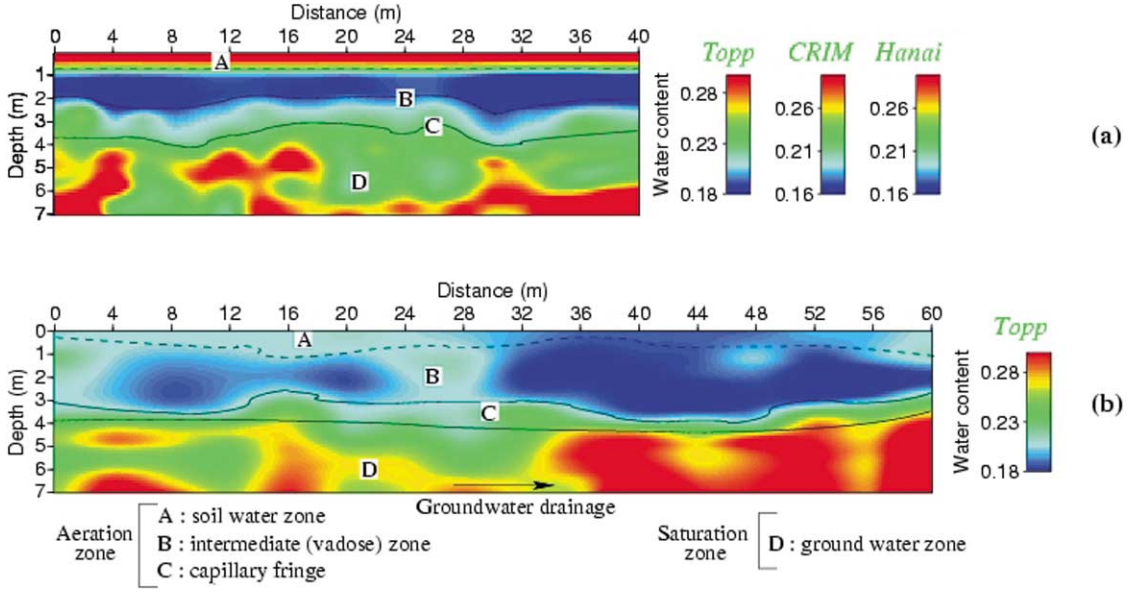
Distance (m)
Depth (m)
A
B
C
D
Topp
CRIM
Hanai
Water content
(a)
Distance (m)
Depth (m)
Topp
Water content
(b)
Groundwater drainage
Aeration zone
A : soil water zone
B : intermediate (vadose) zone
C : capillary fringe
Saturation zone
D : ground water zone

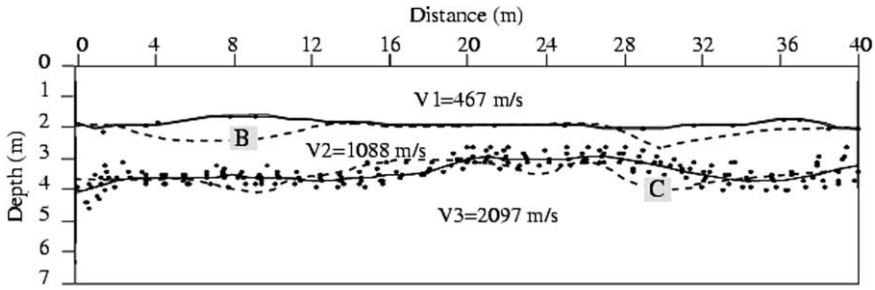

Fig. 6. 2D P-wave velocity model obtained after inversion of the first arrival time in the refraction experiment (experiment A). The dots represent the incident and emergent refraction points along the interface, for all point-source and receiver positions. The dotted lines represent the horizons B and C deduced from GPR multioffset.

approximately 1 m depth presenting a mean water content of 28%, which does not appear as clearly in Fig. 5b. This zone (denoted A), which is adjacent to the surface, is highly affected by conditions at the ground surface (mostly by seasonal and diurnal fluctuations of precipitation, air temperature and air humidity). Experiment A was conducted after strong precipitation, and the soil in this zone was almost saturated (infiltration process), contrary to Experiment B, which was conducted on dry soil. These surface conditions can explain the fluctuations obtained from GPR analysis in this near-surface zone. Fig. 5a shows that this zone is followed by a layer (denoted B) going from 1 m depth to 2.5 m depth with a 17% mean water content, that we interpreted as the intermediate (vadose) zone presenting lateral variations. This zone appears to extend deeper in Fig. 5b, but we can observe the same relative lateral variations as in Fig. 5a (higher water content around positions of $x = 0$ to $x = 2$ m and $x = 22$ to $x = 28$ m). We can also distinguish another intermediate zone, denoted C, which presents a gradual increase in moisture content with depth (between 2.5–3 and 4 m depth). We interpreted this zone, whose upper limit has an irregular shape, as the capillary fringe. It appears thicker in experiment A during the water infiltration process. Finally, the last layer, denoted D, is interpreted as the ground water, a zone where the pores are saturated and that presents a mean water content around 25–26%. It is noticeable that the transition between the capillary fringe and the saturated layer does not appear very clearly throughout the length of the model (especially between positions of $x = 18$ and $x = 28$ m). A discussion about the consistency of these results with those obtained from seismic methods will follow below. It is advisable in any case, as pointed out by Greaves et al. (1996), to consider such images as relative changes of the water content rather than absolute values.

3. Information from P and S-wave data

Seismic refraction and reflection methods have been used successfully for mapping water tables and aquifers in unconsolidated sandy formations. The effect of saturation and pore fluids on seismic velocities has been extensively studied both theoretically (Gassmann, 1951; Biot, 1956, 1962) and experimentally (Domenico, 1974; Murphy, 1984). Bachrach and Nur (1998), using high-resolution field experiments in sands, have recently confirmed the potential of seismic waves to provide a real-time image of the hydrological process. In particular, they showed that, both the reflections and refractions are influenced by partial saturation and do not follow the phreatic surface and that the wave velocity in porous sand can be inverted directly into water saturation. In this section, we want to assess the advantages of using seismic methods to create images of depth interfaces and to get information about the fluid content of near-surface layers. This quantitative information will then be compared to those of GPR.

3.1. Seismic data analysis

In February, 1999, we conducted high-resolution P-wave seismic refraction, P-wave reflection and S-wave reflection experiments in the Anglade test site, to

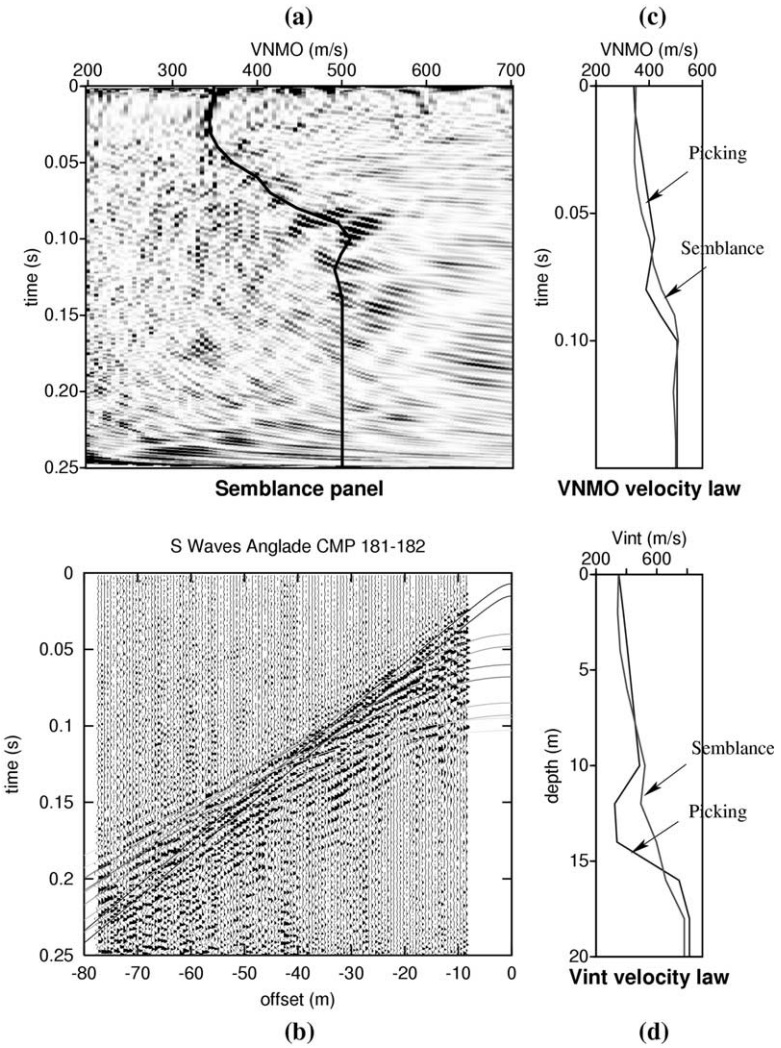

Fig. 7. S-wave reflections analysis for experiment A: estimates of S-wave velocities were performed using the same process than the one used for GPR multioffset data, i.e. NMO velocity extraction from a semblance analysis of reflected S-waves (a), and from a manual time picking (b). (c) NMO velocity models (c) and (d) interval velocity models calculated using the Dix formula (d).

gather information about both P and S-wave velocities at different depths (experiment A). The acquisition of refraction data was conducted using several 50-Hz vertical geophones (48) located every 1 m along a profile centred around the 100 MHz GPR profile (see Fig. 1b). Seven shots (hammer blows) were recorded for every 12 m. The picking of first breaks for each record shows three major slopes, namely, the direct P-wave and two refracted waves. The inversion of the time breaks was performed using the delay-time method (Parkiser and Black, 1957) to obtain a tentative model, which was refined by a ray tracing process and adjusted after various iterations to minimize the variations between experimental and modeled data in a least square sense (Scott, 1973). The obtained model presented in Fig. 6 clearly shows three almost horizontal layers whose velocities increase with depth (from top to bottom 467, 1088 and 2097 m/s, respectively). The superimposition of horizons B and C deduced from GPR multioffset (dotted lines) shows a good consistency between the seismic and GPR methods. There are some deviations, which disappear

Table 1
Properties used to compute seismic velocities (bulk moduli K and densities ρ) of quartz, water and air (denoted by subscripts s, w and a, respectively)

Properties	K_s (GPa)	K_w (GPa)	K_a (GPa)	ρ_s (kg/m^3)	ρ_w (kg/m^3)	ρ_a (kg/m^3)
Sand gravels	35	2.27	0.00015	2.6	1	0.0012

near the centre of the profile, where the 400 MHz antenna has been used to provide supplemental information near the surface. Therefore, we suspect that these weak deviations are due to the EM velocity heterogeneity near the surface, which appears clearly on experiment B (Fig. 5b). The difference in resolution of these methods can also induce such deviations.

The similarity can be explained by geological and/or mineralogical considerations. Nevertheless, as the water content plays a major role for the different physical parameters influencing the seismic velocities and to an even greater extent the dielectric permittivity, we believe that hydrologic parameters are the most likely explanation for this consistency.

The seismic P-wave reflection profile does not give information at a depth of less than about 20 m. This is not the case for the S-wave reflection profile, which has been conducted under an SH configuration, using several 50-Hz horizontal geophones (60) every 0.6 m, and a prototype horizontal vibrator (OYO GEOSPACE), which sweeps from 30 to 300 Hz. Around 150 shots have been recorded, the geophones being fixed and centred on the GPR profile, with offsets ranging from 0.3 to 80 m. Fig. 7b displays a CMP gather obtained at the centre of the refraction profile, where reflected waves can be identified and analyzed using two different methods. The first consists of manually identifying the hyperbolae associated to each reflection (Fig. 7b). The second consists of a semblance spectra analysis, as already discussed for GPR radar data (Fig. 7a). In any case, from these estimations, NMO velocity model can be deduced, and the application of Dix formula (2) yields an interval velocity versus depth relationship. The two velocity models obtained are similar, especially in the near-surface zone (0–5 m depth), where the S-wave velocity (centred around 370 m/s) does not show strong variations (Fig. 7c and d).

3.2. Biot–Gassmann model predictions

Combining information obtained from P-wave refraction and S-wave reflection profiles provides estimates on some properties of the porous layers. The presence of a strong P-wave velocity contrast, associated with the absence of a corresponding S-wave velocity contrast around 3–4 m depth, can be explained by saturation variations. Indeed, as predicted by the Biot–Gassmann theory or measured by ultrasonic velocity experiments (as performed on Massilon sandstones by Murphy (1984)), and by field experiments in sand by Bachrach and Nur (1998), S-wave velocity is almost insensitive to water saturation when the saturating fluid is composed of an air–water mixture. In opposition, P-wave velocity greatly increases when water saturation reaches 100%. Using the Biot–Gassmann theory, which will not be reviewed here (see e.g. Pride et al., 1992; Bachrach and Nur, 1998), it is possible to assess some soil properties using S-wave and P-wave velocities as a function of saturation variations. In a water–rock mixture, the slight decrease of both P and S-wave velocities, when water saturation remains lower than a certain value, which can reach 99%, may be due to density effects. When the water saturation exceeds this value, it is well-known that there is a strong increase of P-wave velocity due to a jump in the fluid frame modulus of the considered material. We think that such a mechanism can explain the observed P-wave velocity contrasts in our test site, as the transition from a partially saturated to a fully saturated layer.

In addition to the saturation jump, seismic velocities mainly depend on porosity and consolidation of the frame material, via its frame bulk and shear moduli (Murphy et al., 1993). By assuming the third layer to be water saturated, an inversion process of both S and P-wave velocity changes as a function of these three properties can be better constrained. There is no explicit form of the inversion process leading to porosity estimates of the saturated layer as a function

of velocity. We applied the well-known poro-elastic velocity model derived from the Biot–Gassmann theory (e.g. Bachrach and Nur, 1998) using the bulk modulus K and the density ρ of quartz, water and air displayed in Table 1.

If a 2% confidence estimate is assumed for these velocities, the solution space is quite restricted. We found in this case that porosity ranges from 0.23 to 0.26, frame shear modulus (G_{fr}) ranges from 0.3 to 0.31 *GPa* and frame bulk modulus (K_{fr}) ranges from 2 to 2.26 GPa. Unfortunately, the estimation of seismic velocities is not precise enough to constrain the saturation transition (the saturation in the second layer). Note that the porosity estimates are consistent with those predicted by GPR radar data (mean porosity of 0.25–0.26). Moreover, the access to relatively precise soil consolidation estimates can be very interesting, particularly in civil engineering or for horizontal borehole applications. The present study shows the potential of high-resolution P and S-wave reflection methods to identify properties of aquifers in a porous medium at greater depth as compared to the use of the GPR method.

4. Water conductivity estimations from combined electric and GPR data

Electrical surveys measure the distribution of electrical currents generated by an applied direct electric field and are interpreted in terms of the apparent resistivity of the ground. Electrical monitoring techniques have been used successfully for environmental purposes because of their ability to observe the change in resistivity due to migration of contaminants and/or water in the vadose zone (e.g. Greenhouse and Harris, 1983; Kean et al., 1987; Van et al., 1991).

The dipole–dipole array provides both lateral and vertical coverage of the ground. A sequence of source dipoles of length a and receiving dipoles of the same length are laid out on the ground. By varying the spacing between the dipoles, their length, and by moving the array laterally over the ground, it is possible to construct an electrical pseudo-section of the subsurface. This can be inverted to calculate a 2-D resistivity (or conductivity) model of the ground.

4.1. Conductivity law in unsaturated porous media

At low frequencies ($f < 10^3$ Hz), grain or gas phases can be considered as insulator material as compared to an electrolyte. In this case, the macroscopic conductivity of porous rocks results from two mechanisms: (i) bulk conduction which represents electromigration of the ions in the interconnected pore space, and (ii) surface conduction resulting from various conduction processes near the interface separating the pore fluid from the grains, where an electric double layer develops (Pride, 1994; Revil and Glover, 1997). This macroscopic effective conductivity σ can be expressed as (Guéguen and Palciauskas, 1992; Pride, 1994)

$$\sigma = \frac{1}{F}\left(\sigma_w + 2\frac{\sigma_s}{\Lambda}\right). \tag{8}$$

Here F is the formation factor taking into account microscopic reduction processes associated to the tortuous way of electric charges migration in the fluid phase, σ_w represents the fluid conductivity, σ_s denotes the surface conductivity, and Λ a characteristic length of the pore space microgeometry. As the presence of clay sediments in our test site is limited, we will assume in the following that the contribution of surface conductance can be ignored. Therefore, the effective conductivity depends only on the electrolyte's conductivity and on the microstructure of the mixture, via the formation factor F.

The formation factor F characterizes the reduction in conductivity of a water volume that is caused by the presence of a non-conducting matrix and/or of an insulating second fluid phase (or gas). For clean water-saturated sands and sandstones, an expression relating the formation factor F to the effective porosity ϕ

$$F = \phi^{-m}, \tag{9}$$

was experimentally obtained by Archie (1942). The empirical exponent m can be close to 1 in the case of cracked granite, and is more typically in the range of $1.5 \leq m \leq 2.5$ for sedimentary rocks (for granular sediments, $m \leq 1.5$). This value depends strongly on the pore microgeometry, particularly on tortuosity (which changes with porosity) and on lithology. It is possible to account for the partial saturation case (air/water mixture), by considering the gas phase and rock

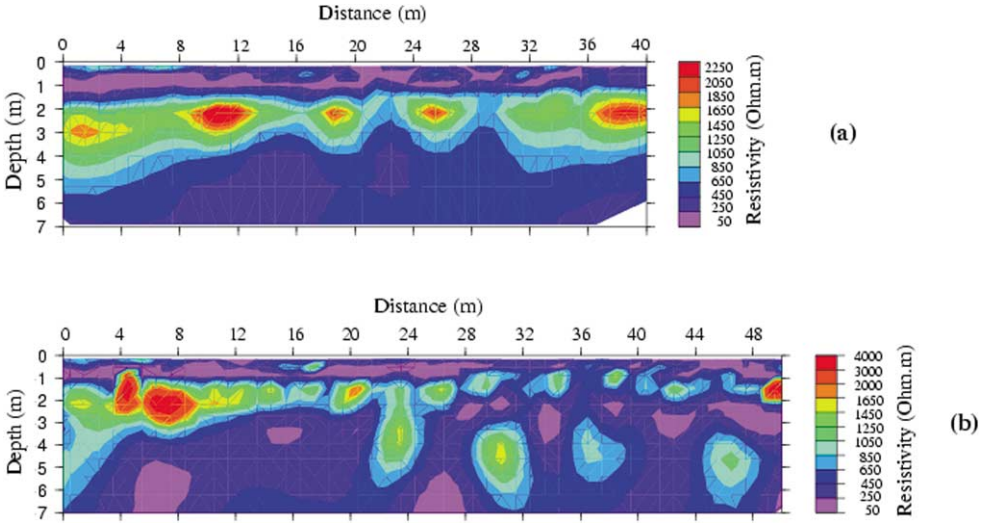

Fig. 8. 2D electrical resistivity models obtained after the inversion of apparent resistivity measurements acquired in the dipole–dipole configuration for experiments A (a) and B (b).

matrix as insulators. When surface conductance is neglected, an extension of Archie's law (see, e.g. Waxman and Smits, 1968) leads to

$$\sigma = S_w^n \phi^m \sigma_w, \tag{10}$$

where the saturation exponent n is a function of the microgeometry of the gas/water mixture. The efficiency of extended Archie's law has been confirmed by many experimental studies when rocks have a low-clay content, and particularly when the fluctuations of microporosity and microsaturation are small, which is not the case for chemically unstable rocks, such as carbonates (Sen, 1997). In general, the determination of m and n can only be

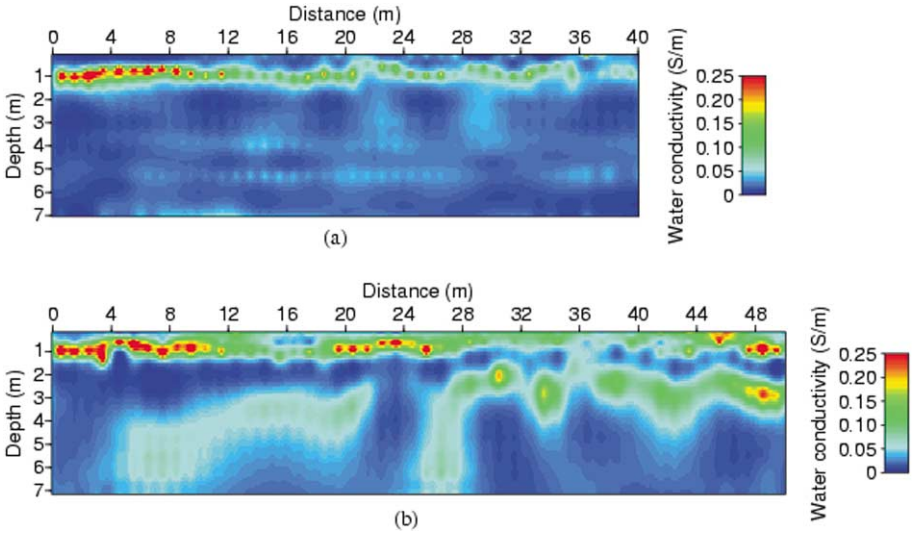

Fig. 9. 2D models of water conductivity estimates obtained by replacing the 2D electrical bulk resistivity models and the volumetric water content influence, which was estimated through multioffset GPR data in the Archie equation. The cementation exponent of the extended Archie's law is assumed to be equal to $m = n = 2$. (a) Experiment A. (b) Experiment B.

achieved by laboratory experiments. Yaramanci and Flach (1992) obtained a good consistency between empirical predictions of rock conductivity computed using $m = n = 2$ in Eq. (10), and measurements on rock-salt samples. In practice, the values $m = n = 2$ are often adopted for various types of rocks (e.g. Edwards, 1997; Dannovski and Yaramanci, 1999).

4.2. Water conductivity model

The 2D electrical profiles, centred around the CMP radar profile in the Anglade test site (Fig. 1b), were acquired using 64 electrodes (experiment A) and 80 electrodes (experiment B) spaced every 1 m using the dipole–dipole configuration. The program RES2DINV (Loke and Barker, 1996), based on the smoothness-constrained least-squares method (deGroot-Hedlin and Constable, 1990), was used in order to invert the 622 and 1028 resistivity measurements acquired for experiments A and B, respectively. The 2D resistivity models obtained after 7 iterations with a final RMS error below 2.6%, are displayed in Fig. 8. The resistivity sections show clearly an alternation of horizontal layers with high and low resistivities. A laboratory resistivity measurement performed on the 1 m depth soil sample located at a position of $x = +3$ m along the profile during experiment B displays a resistivity of 250 Ohm m^{-1}, which presents a good consistency with the value proposed after the inversion process (Fig. 8b).

The horizontally and vertically varying resistivity and water content models (obtained from Topp equation) are combined using Archie's law (Eq. (10)). We only present the water conductivity estimates obtained from Archie's law using $m = n = 2$ for both experiments (Fig. 9), although we also computed Archie's law with different values of m and n ranging from 1 to 2.5. In fact, the absolute estimates of water conductivity were highly fluctuating as a function of m and n, which was not the case of the relative images presenting a higher stability. This fact indicated that soil moisture variations can be considered as second-order effects compare to water conductivity variations into Archie's law.

Both models show a higher water salinity intrusion near the surface, and possible salinity transfers along preferential zones at depths. Below 1.2 m depth, except in the preferential flow zones, the water conductivity appears relatively homogeneous. These results will be interpreted more precisely in Section 5.

5. Discussion

We shall briefly discuss the water content and water conductivity distributions obtained from GPR measurements and its combination with electrical and seismic measurements, respectively.

The use of multioffset GPR data to estimate the soil water content has been shown to be reliable, and can replace extensive sample analysis.

Three to four quasi-horizontal layers can be recognized from GPR data (Fig. 5a) and three similar layers are observed in seismic refraction studies (Fig. 6). This illustrates the advantage of combining different methods which are based on different physical parameters and possess different sensitivity and resolution. In our case, it is not possible to determine if the seismic contrasts are due to mineralogy, consolidation or water content changes. Only a combined analysis of GPR and seismic results clearly identifies the water table around 4 m depth and its lateral fluctuations (which do not appear very clearly in some zones on Fig. 5a and b, using GPR only).

Nevertheless, in another test site, one can encounter some formations where the transition zone does not yield strong seismic reflected or refracted waves. In the same way, there are some regions where the identification of the transition zone is easier by GPR, because of the strong EM reflected waves.

From the high resolution GPR measurements even the capillary fringe is observed (Fig. 5a) which does not appear on seismic interpretation (the gradient in velocity appears to be too weak). There is a satisfactory consistency in quantitative water content predictions of the saturated layer when analyzing both GPR and seismic velocities using the Biot–Gassmann theory.

Finally, we would like to emphasize that GPR can monitor accurately both lateral and vertical water content variations, and that such large-scale images, if repeated over time, should help hydrologists to map and interpret water transfers and preferential flow paths in the vadose zone during infiltration, as well as water movement, both qualitatively and quantitatively. By using higher-frequency antennas, the higher

Table 2
Chemical analysis of a water table sample (ppm) in experiment B

Anions/cations	Ca^{++}	Mg^{++}	Na^{++}	K^{+}	NH_4^{+}	Cl^{-}	NO_3^{-}	SO_4^{--}
	81	4.5	2.8	1.4	0.15	3.5	9.9	11

resolution images of water content will provide useful applications in various domains, such as studies on the water absorption by plants, although the penetration depth will decrease.

For the water conductivity models presented on Fig. 9, the first point concerns the reliability of the quantitative values. The water sample analysis conducted in a well during experiment B indicates a water conductivity of 45 mS/m. The average water conductivity obtained using Archie's law, shows an almost constant water conductivity of 40 mS/m from 1.4 m depth. It is important to note that if we had used a value of $m = n = 1.5$, the mean constant water conductivity under 1.4 m depth would have been 8 mS/m.

It is also noticeable that the mean bulk resistivity presents strong variations between 1 to 4 m depth in both experiments, as well as the water content in this zone. After applying Archie's law, the water conductivity appears almost constant in this zone, thus emphasizing the role of soil moisture on bulk resistivity and the validity of Archie's law. It also illustrates the advantage of combining two geophysical methods. Otherwise, the resistivity increase at 2 m could have been interpreted as due to mineralogic variations. Both 2D water conductivity models (Fig. 9) display a high conductivity zone between 0.4 and 1.2 m, which varies laterally and does not show significant fluctuations as a function of time. A key question is the origin of this high concentration zone: is it due to artifacts in the proposed methodology, to natural or to anthropological causes? As discussed before, the employed methodology seems to give consistent results with sample analysis beyond 1.2–1.4 m depth. For the near-surface area, there may be two causes that could lead to errors in water conductivity estimates. Firstly, as we used 100 MHz antennas for GPR measurements, the resolution near the surface is poor and thus water content estimates in this zone only provides a mean water content from the surface to the first reflection (occurring around 1 m depth). If there is a water infiltration process in the soil, the vertical infiltration front can modify water conductivity estimates. As this high water conductivity zone appears in both experiments, where surface conditions were extremely different, this explanation seems unsatisfactory. The most likely explanation of this higher conductivity is the presence of a higher concentration of clay in the first soil (to 1.2 m depth, as observed from sample measurements presented in Fig. 1c). This clay content can generate artifacts in water conductivity estimates, because the contribution of surface conductances to the bulk conductivity is no more negligible, and the choice of $m = n = 2$ may be less convenient, Archie's law is no longer applicable. In this case, the water conductivity estimates using Archie's law represent mainly an apparent water conductivity and no longer the intrinsic water conductivity, which will be much lower depending on the clay content of the formation, as proposed by Keller (1987). Moreover, such a surface conductance, resulting from cations adsorption (carbonates), can explain the high value of the pH measured on a 1 m depth soil sample (pH = 7.85). The adsorptive properties of these clays (composed of 58% of illite, 23% of chlorite, 11% of kaolinite and 7% of interstratified), can lead to trap salts which tend to concentrate in the root zone due to the twin processes of evaporation and transpiration, and thus participate to an increase in conductivity. The weak lateral heterogeneity observed in both experiments (Fig. 9), which is stable over time, can thus be due to heterogeneity, common in this alluvial context where fluvial streams have been observed.

We also tested another possibility, i.e. the impact of the agricultural activity. The ground water sample analysis conducted during experiment B (Table 2) showed that the concentration of nitrates, sulphates or chlorides were normal. It is also noticeable that no unusual proportion of nitrates were measured on the 1 m depth soil sample, making this hypothesis unrealistic.

Therefore, the textural formation of deposits and its fluctuations, combined with the adsorptive properties of clays, can explain the water conductivity anomalies observed in the uppermost soil layer. Moreover, such a hypothesis can explain the stability of these anomalies over more than one year.

Fig. 9 also highlights preferential flows, below a depth of 1.5 m down to the water table, which varies a lot over time. In fact, during its passage through the soil, the infiltrated water tends to dissolve additional solutes, including products of mineral and organic matter, as well as residues of fertilizers and pesticides. As they move vertically, solutes are adsorbed, taken up by plants and react among themselves. These phenomena depend on different parameters, including water transfer, temperature, acidity, which fluctuate with time. Our proposed model can be considered as a rough estimate of these transfers in the soil. Such large scale images are important for the understanding or interpreting both qualitatively and quantitatively of these transfers. They can be applied to contaminated areas, to assess the quality of aquifers used for human consumption, and/or to monitor the efficiency of eventual remediation methods with very limited drilling.

6. Conclusion

In this research, we used a multioffset GPR data set to estimate the water content of near-surface rocks over an area of 40×7 m, with a satisfactory resolution, in a fast and non-destructive manner. The obtained results are consistent both geometrically and quantitatively with those deduced from various seismic methods. The seismic methods benefited from strong reflections and refractions within the unsaturated vadose zone. We emphasize that a GPR study is easy to conduct in the field (and will now be even easier with the use of multichannel GPR systems). By repeating these measurements over time, it is possible to follow the fluctuation of aquifers and water content in response to natural and/or anthropological impacts. It can therefore be a valuable tool for hydrological purposes.

Using the obtained water content estimates, we were able to propose a solution to the problem of trade-off between bulk and water conductivities. For that we needed the additional assumption that grain surface conductances could be neglected. As a result, we obtained an image of ionic water transfer based on electrical and multioffset GPR measurements, that permitted access to geochemical information on a large scale. This information, in turn, can be used to track natural chemical reactions and/or monitor possible ionic contaminants in situ. If the relative image can be considered as reliable, the absolute water conductivity estimates highly depend on the cementation exponents used in Archie's law, and should not be considered. This is also a consequence of the complexity of the parameters involved and of the lack of calibrating existing empirical or theoretical models with macroscopical sample data. These problems concern the sensitivity of the dielectric permittivity and the bulk conductivity to the water content and to a certain degree, to the ionic concentrations. It would be preferable in future to refine this calibration, but the overall approach used here appears very useful, especially when considering the time variation of the measured geophysical parameters.

Acknowledgements

We are grateful to S.A. al Hagrey and to an anonymous reviewer for their comments which greatly improved the manuscript. We also thank C. Doussan from INRA of Avignon, D. Cussey and R. Sabrier from Pau University for helpful discussion, A. Daudignon, B. Fasentieux and E. Landat for sample analysis, as well as all those who helped us with field experiments. S. Garambois and P. Sénéchal thank Elf Exploration Production for their financial support. The S wave experiment was made possible thanks to the help of J. Muller, from Elf Exploration Production.

References

Archie, G.E., 1942. The electrical resistivity log as an aid in determining some reservoir characteristics. Trans. AIME 145, 54–62.

Bachrach, R., Nur, A., 1998. High-resolution shallow-seismic experiments in sands, Part I: Water table, fluid flow and saturation. Geophysics 63, 1225–1233.

Biot, M.A., 1956. Theory of propagation of elastic waves in fluid saturated porous solid. I low frequency range, II higher frequency range. J. Acoust. Soc. Am. 28, 168–191.

Biot, M.A., 1962. Mechanics of deformation and acoustic propagation in porous media. J. Appl. Phys. 33, 1482–1498.

Charlton, M., 2000. Small-scale soil-moisture variability estimated using ground penetrating radar. Proceedings of Eighth International Conference on Ground Penetrating Radar, Gold Coast, Australia, 23–26 May 2000, pp. 798–804.

Dannovski, G., Yaramanci, U., 1999. Estimation of water content and porosity using combined radar and geoelectrical measurements. Eur. J. Environ. Engng Geophys. 4, 71–85.

Davis, J.L., Annan, A.P., 1989. Ground penetrating radar for high-resolution mapping of soil and rock stratigraphy. Geophys. Prospect. 37, 531–552.

deGroot-Hedlin, C., Constable, S., 1990. Occam's inversion to generate smooth, two dimensional models from magnetotelluric data. Geophysics 55, 1613–1624.

Dix, C.H., 1955. Seismic velocities from surface measurements. Geophysics 20, 68–86.

Domenico, S., 1974. Effect of water saturation on seismic reflectivity in sand reservoirs encased in shale. Geophysics 39, 759–769.

Dvorkin, J., Nur, A., 1998. Time-average equation revisited. Geophysics 63, 460–464.

Edwards, R.N., 1997. On the resource evaluation of marine gas hydrate deposits using sea-floor transient electric dipole–dipole methods. Geophysics 62, 63–74.

Endres, A.L., Knight, R., 1992. A theoretical treatment of the effect of microscopic fluid distribution on the dielectric properties of partially saturated rocks. Geophys. Prospect. 40, 307–324.

Fisher, E., McMechan, G.A., Annan, A.P., 1992. Acquisition and processing of wide-aperture ground-penetrating radar data. Geophysics 57, 495–504.

Freedman, R., Vogiatzis, J.P., 1979. Theory of microwave dielectric constant logging, using the electromagnetic propagation method. Geophysics 44, 969–986.

Gassmann, F., 1951. Über die Elastizität poröser Medien. Vierteljahrschr. Naturforsch. Gesellschaft, Zürich 96, 1–23.

Greaves, R.J., Lesmes, D.P., Lee, J., Toksöz, N.M., 1996. Velocity variations and water content estimated from multi-offset, ground-penetrating radar. Geophysics 61, 683–695.

Greenhouse, J.P., Harris, R.D., 1983. Migration of contaminants in groundwater at a landfill: A case study. 7. DC, VLF, and inductive resistivity surveys. J. Hydrol. 63, 177–197.

Guéguen, Y., Palciauskas, V., 1992. In: Hermann (Ed.). Introduction à la Physique des Roches. p. 299.

Hagrey, S.A.al, Müller, C., 2000. GPR study of pore water content and salinity in sand. Geophys. Prospect. 48, 63–85.

Kean, W.F., Walter, M.J., Layson, H.R., 1987. Monitoring moisture migration in the vadose zone with resistivity. Ground Water 25, 562–571.

Keller, G.V., 1987. Rock and mineral properties. In: Nabighian, M.N. (Ed.). Electromagnetic Methods in Applied Geophysics. Series: Investigations in Geophysics 3, vol. 1. Society of Exploration Geophysics, Tulsa, Oklahoma.

Loke, M.H., Barker, R.D., 1996. Rapid least-squares inversion of apparent resistivity pseudosections using a quasi-Newton method. Geophys. Prospect. 44, 131–152.

Murphy III, W.F., 1984. Acoustic measures of partial gas saturation in tight sandstones. J. Geophys. Res. 89, 11549–11559.

Murphy III, W.F., Reisher, A., Hsu, K., 1993. Modulus decomposition of compresional and shear velocities in sand bodies. Geophysics 58, 227–239.

Parkiser, L.C., Black, R.A., 1957. Exploring for ancient channels with the refraction seismograph. Geophysics 22, 32–47.

Pride, S.R., 1994. Governing equations for the coupled electromagnetics and acoustics of porous media. Phys. Rev. B 50, 15678–15696.

Pride, S.R., Gangi, A.F., Morgan, D.F., 1992. Deriving the equations of motion for porous isotropic media. J. Acoust. Soc. Am. 92, 3278–3290.

Revil, A., Glover, P.W.J., 1997. Theory of ionic surface electrical conduction in porous media. Phys. Rev. B 55, 1757–1773.

Scott, J.H., 1973. Seismic refraction modeling by computer. Geophysics 38, 271–284.

Sen, P.N., 1997. Resistivity of partially saturated carbonate rocks with microporosity. Geophysics 62, 415–425.

Sen, P.N., Scala, C., Cohen, M.H., 1981. A self-similar model for sedimentary rocks with application to the dielectric constant of fused glass beads. Geophysics 46, 781–795.

Shen, L.C., Savre, W.C., Price, J.M., Athavale, K., 1985. Dielectric properties of reservoir rocks at ultra-high frequencies. Geophysics 50, 692–704.

Topp, G.C., Davis, J.L., Annan, A.P., 1980. Electromagnetic determination of soil water content: measurements in coaxial transmission lines. Water Resour. Res. 16, 574–582.

Van, G.P., Park, S.K., Hamilton, O., 1991. Monitoring leaks from storage ponds using resistivity methods. Geophysics 56, 1267–1270.

Van Overmeeren, R.A., Sariowan, S.V., Gehrels, J.C., 1997. Ground penetrating radar for determining volumetric water content; results of comparative measurements at two test sites. J. Hydrol. 197, 316–338.

Waxman, M.H., Smits, L.J.M., 1968. Electrical conductivities in oil-bearing shaly sands. Soc. Pet. Engng J. 8, 107–122.

Weiler, K.W., Steenhuis, T.S., Boll, J., Kung, K.-J.S., 1998. Comparison of ground penetrating radar and TDR as soil water sensors. Soil Sci. Soc. Am. J. 62, 1237–1239.

Yaramanci, U., Flach, D., 1992. Resistivity of rock-salt in ASSE (Germany) and petrophysical aspects. Geophys. Prospect. 40, 85–100.

Yilmaz, O., 1987. Seismic Data Processing. Society of Exploration Geophysics, Tulsa.